Int. J. Heat Mass Transfer. Vol. 34, No. 3, pp. 795–808, 1991
Printed in Great Britain

0017–9310/91 $3.00 + 0.00
© 1991 Pergamon Press plc

Numerical simulation and field testing of flame-jet thermal spallation drilling—1. Model development

RICK M. RAUENZAHN† and JEFFERSON W. TESTER
Department of Chemical Engineering, Massachusetts Institute of Technology, Cambridge, MA 02139, U.S.A.

(*Received* 7 *June* 1989 *and in final form* 10 *May* 1990)

Abstract—Certain polycrystalline rocks will fracture into thin, disk-like fragments when exposed to rapid surface heating. Some current hard-rock drilling methods using supersonic flame-jets as heat sources exploit this behavior for efficient granite quarrying or blasthole formation. Recent extensions of Weibull's theory of rock failure to quantitatively analyze rock spallation are employed to estimate spall size distributions and rock surface temperatures at the onset of spallation. A numerical drilling simulation code incorporating rock failure criteria and turbulent flow effects is developed to predict spallation rates and hole radii under field-drilling conditions. Because an accurate description of heat transfer through a turbulent wall jet is required, the wall-function method is generalized in a crude way to account for compressible flow past roughened, non-adiabatic rock surfaces.

INTRODUCTION

CONVENTIONAL methods for drilling and tunneling have relied exclusively on mechanical rock breakage, often with compressively loaded bits supplying the required stress. Primary disadvantages of these mechanical methods are bit and drill pipe wear and the large capital expense associated with the drilling rig and ancillary equipment. When hard, crystalline, basement rocks such as granite are encountered, crushing and grinding of rock are very arduous, leading to low instantaneous penetration rates (1–7 m h^{-1}) [1, 2], rapid bit wear, and frequent bit replacements. Hardened materials, such as synthetic diamonds and tungsten carbide, have significantly improved bit durability and penetration speeds, but rotary drilling remains a slow, costly, hardware-intensive process.

Thermal rock destruction methods use rapid heat transfer to induce thermal stresses leading to rock failure. Radiative heat sources from lasers or electron beams or convective heating from flame- or plasma-jets have been tested in experimental drilling programs [1, 3]. Although radiative or electrical power supplies can readily provide enough energy to penetrate a rock working face by melting or spalling, they provide no means of clearing the rock rubble as it is produced. Flame-jet spallation drilling, or, synonymously, jet piercing, employs a hot jet of combusting fuel and oxidant, usually flowing at supersonic speeds and directed at underlying rock (Fig. 1). The momentum of the exhaust gases provides sufficient energy to remove the spalls. Spallation drilling concepts and hardware have been tested and applied in the field with diesel oil as the fuel and either air or pure oxygen as the oxidant [1].

Rock spallation mechanisms have been the subject of many experimental and theoretical studies of rock failure under intense heating conditions (see refs. [4, 5] for reviews). Recently, application of Weibull's statistical failure theory to rock spallation has led to a new method of predicting rock spallation characteristics. Spallation initiation mechanisms and relationships formulated in refs. [5, 6] are applicable, regardless of heating mode, to any thermal spallation drilling

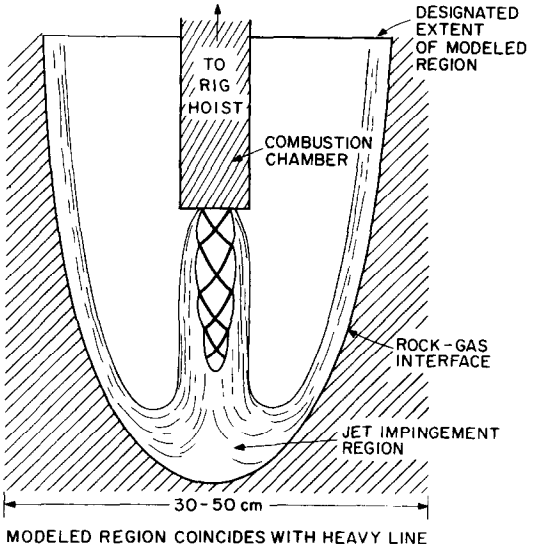

FIG. 1. Physical model of downhole region during spallation drilling. Supersonic jet expands through nozzle throat and impinges on underlying rock, causing spallation. Modeled region extends to include most of the spalling surface.

† Current address: Theoretical Division, Los Alamos National Laboratory, Los Alamos, NM 87545, U.S.A.

NOMENCLATURE

A, B constants in Van Driest's generalized velocity formula
A_h horizontally projected cell face area [m^2]
A_v vertically projected cell face area [m^2]
c speed of sound [m s^{-1}]
c_{jet} speed of sound at nozzle throat conditions [m s^{-1}]
C_1, C_2, C_μ constants in turbulent transport and viscosity relationships
C_L chip aspect ratio (diameter divided by thickness)
C_p heat capacity at constant pressure [J kg^{-1} K^{-1}]
$C_{p,jet}$ heat capacity at constant pressure at jet inlet temperature [J kg^{-1} K^{-1}]
$C_{p,r}$ rock heat capacity [J kg^{-1} K^{-1}]
C_v heat capacity at constant volume [J kg^{-1} K^{-1}]
E Young's modulus [Pa], total fluid energy [J kg^{-1}], constant in law of the wall velocity profile
F constant in law of the wall temperature profile
$\langle h \rangle$ effective averaged surface heat transfer coefficient from flame-jet [W m^{-2} K^{-1}]
h_c asperity dimension of roughened surface [m]
h_δ effective heat transfer coefficients across roughness [W m^{-2} K^{-1}]
I fluid internal energy [J kg^{-1}]
I_{jet} jet internal energy at nozzle throat [J kg^{-1}]
k turbulent kinetic energy [J kg^{-1}]
k_f fluid thermal conductivity [W m^{-1} K^{-1}]
k_{jet} incoming jet turbulent kinetic energy [J kg^{-1}]
k_p turbulent kinetic energy at the cell center proximate to the wall [J kg^{-1}]
k_r rock thermal conductivity [W m^{-1} K^{-1}]
l_t turbulent length scale [m]
m Weibull homogeneity parameter
M Mach number
M_∞ freestream Mach number
n normal distance and coordinate [m]
p fluid pressure [Pa]
p' fluctuating pressure [Pa]
$\bar{p}$ time-averaged pressure [Pa]
p_{jet} jet pressure at nozzle throat [Pa]
p_0 ambient pressure [Pa]
Pr molecular Prandtl number
Pr_t turbulent Prandtl number
Q heat flux [W m^{-2}]
$\langle Q \rangle$ spatially averaged, bottom hole heat flux [W m^{-2}]
Q_f, Q_w wall heat flux from fluid turbulent boundary layer [W m^{-2}]
r radial coordinate
δr radial spatial increment [m]
R_{ij} Reynolds stress [Pa]
R_{dr} radius of flame-jet drill nozzle [m]
Re_c Reynolds number based on friction velocity and asperity dimension
R_h hole radius [m]
St Stanton number
$\langle St \rangle, \langle St \rangle_{eff}$ effective spatially averaged Stanton number
St_c Stanton number for fluid in roughness cavities
t time [s]
δt temporal increment [s]
T^+ dimensionless temperature within law of the wall
δT_0^+ St_c^{-1}
T_f fluid temperature [K]
T_{jet} jet temperature [K]
T_r rock temperature [K]
T_{r0} initial rock temperature [K]
T_w rock wall surface temperature [K]
T_∞ freestream temperature [K]
u, v fluid velocity in radial, axial direction [m s^{-1}]
$\mathbf{u}$ fluid velocity vector [m s^{-1}]
$\bar{u}, \bar{v}$ time-averaged velocity [m s^{-1}]
u', v' fluctuating component of velocity [m s^{-1}]
u^+ dimensionless velocity within law of the wall profile
u_p velocity at cell center nearest wall [m s^{-1}]
u_r local rock penetration velocity [m s^{-1}]
v_{jet} jet velocity at nozzle throat [m s^{-1}]
V volume [m^3]
V_{dr} overall rock drilling velocity [m s^{-1}]
y^+ dimensionless distance normal flat plate, or, equivalently, Reynolds number based on outward coordinate
z axial coordinate
δz axial spatial increment [m]
Z_{dr} drilling nozzle standoff distance [m].

Greek symbols

α volume fraction of rock chips
α_r rock thermal diffusivity [m^2 s^{-1}]
β_r rock thermal expansion coefficient [K^{-1}]
γ ratio of gas specific heats, C_p/C_v
δ_{ij} Kronecker delta
ε dissipation rate of turbulent kinetic energy [W kg^{-1}]
θ, θ_i inclination angle of boundary
κ von Karman constant

NOMENCLATURE *(continued)*

λ	bulk or longitudinal fluid viscosity [Pa-s]	ρ_0	ambient gas density [kg m^{-3}]
μ	molecular fluid viscosity [Pa-s]	ρ_r	rock density [kg m^{-3}]
μ_t	turbulent viscosity [Pa-s]	ρ_w	gas density at wall conditions [kg m^{-3}]
μ_w	viscosity at wall conditions [Pa-s]	σ_k	effective Prandtl number for diffusion of turbulent kinetic energy
ν	gas kinematic viscosity [m^2 s^{-1}]	σ_ε	effective Prandtl number for diffusion of turbulent kinetic energy
ν_w	kinematic viscosity at wall conditions [m^2 s^{-1}]	σ_0	Weibull rock strength [Pa]
ρ	density [kg m^{-3}]	τ	fluid stress [Pa]
ρ_{jet}	gas jet density [kg m^{-3}]	τ_w	wall shear stress [Pa].

process. What has not been examined in detail are the heat transfer characteristics of flame-jets used to induce thermal spallation and suggestions for improving their performance. Our work has addressed these issues through a combined computational and experimental approach.

Most procedures aimed at optimization of spallation drilling systems are highly empirical and specific to particular field applications. They tend to emphasize engineering details rather than provide fundamental quantitative information about what parameters affect drill performance. Consequently, no universal predictive capability has been established, though recommendations exist for piercing specific rock types (for example, taconite drilling [7]).

Because transfer of heat from hot, turbulent, gaseous products of combustion is responsible for rock spallation, the details of fluid flow near a spalling surface are extremely important. Because higher temperature gradients exist in the rock, one is tempted to ignore behavior of the relatively 'well-mixed' fluid and search for a more complete understanding of the time–temperature response of rock. The heat flux at a rock surface controls removal rate, however, and the direct correspondence between drilling velocity and the heating power delivered is crucial.

Direct measurements of relevant flow quantities (temperature, pressure, velocity) on which heat transfer rate from the gas is most dependent are impeded by severe conditions present and disturbances of the flow field caused by any attempt to record these values. Therefore, development of a physical model of spallation, followed by a mathematical description provides a tractable method of numerically estimating the drilling process variables. The physical model described below is a fairly accurate representation of the actual configuration of the drill nozzle and associated hardware, which sets the geometry for subsequent development of equations for fluid and rock flow. Then, finite-difference formulations are introduced to approximate the differential equations for solution by numerical methods. Restating the independent variables in dimensionless terms eases presentation of the final results, expressed as drilling rate and hole size as functions of jet pressure, temperature, mass flow rate, and nozzle geometry. In Part 2 of this paper, predictions are then compared to actual drilling data gathered by using a scaled-down version of spallation tools employed for commercial hole drilling [5, 8].

MODELING APPROACH

The physical model provides enough detail about downhole geometry and jet configuration and flow patterns to predict trends in drilling efficiency. The kinetics of the actual combustion process and equipment associated with injection of fuel, air, and the function of the cooling water are ignored in our model. In most properly designed combustion chambers, the reaction of fuel and oxidants proceeds to over 95% of completion [9, 10]. Potentially, the equilibrium composition can alter as gas expanding from the high-pressure combustion reservoir cools and dissociated species recombine. However, consideration of any unreacted fuel and oxidant in these relatively low-temperature spallation systems is unnecessary [11]. Thus, the inlet to the flow field in this simulation is assumed to be given by the condition at the sonic throat of the drill nozzle as the completely reacted gases exit into the bottom hole cavity. Any shift in gas equilibrium composition is ignored. The path of the fluid is computationally tracked through the region near the nozzle mouth and the wellbore surface. The rock interface serves as another boundary in the calculational domain and forces the gas and any spalls to exist through the annulus between the drill pipe and previously formed wellbore (Fig. 1). Because of the low solid volume fraction ($\alpha \sim 10^{-4}$), the two-field effects are expected to be very local, and probably are confined to the boundary layer. Wall blowing corrections to the boundary heat transfer will be presented in a following study, but shock–solid interactions in the bulk will be scarce (most computational cells will not, on average, even contain a single rock chip) and are ignored in the present work.

Rock spallation results from thermal stress accumulation and subsequent cracking of rock fabric into thin flakes, or spalls, and is phenomenologically described by a slight modification of Weibull's stat-

istical failure theory [1, 6]. The heating process and introduction of rock chips into the flow field are lumped into a boundary condition. No effort is made within the code to account for the intricacies of each discrete chip liberation during spallation, as the general criteria developed earlier [1] should be sufficiently accurate for these calculations. Furthermore, the generation of dust-sized rock chips (<0.5 mm thick) in a wellbore with a diameter of 8 cm or more does not, to first order, depend on the curved nature of the hole. Spallation criteria used for flat surfaces should be adequate given the separation of length scales. Rock degradation mechanisms during heating are extensively discussed in previous work [1, 5], but the effects of thermally induced microcracking before the onset of spallation are not well understood. Temperature-dependent Weibull constraints would presumably be required in more complete studies of flame-jet drilling [6]. We assume constant values of the Weibull parameters (m and σ_0) for our purposes. Also, the details of heat transfer to the drill housing are treated simplistically, because nearly all of the important flow events occur near the rock–fluid interface. All previous field experimentation has indicated that erosion of the drill pipe and nozzle, not melting induced by external gas flow, is the main wear mechanism [8].

MATHEMATICAL MODEL

The physics of the flow in this confined cavity follows from the laws of continuum mechanics for fluids. The differential equations stating the conservation of mass, momentum, and energy of an axisymmetric compressible one-phase flow of fluid possessing spatially dependent pressure (p), density (ρ), velocities (u, v), and total energy (E) in the absence of body forces are [12]

$$\frac{\partial \rho}{\partial t}+\frac{1}{r}\frac{\partial \rho u r}{\partial r}+\frac{\partial \rho v}{\partial z}=0$$

$$\frac{\partial \rho u}{\partial t}+\frac{1}{r}\frac{\partial \rho u^2}{\partial r}+\frac{\partial \rho u w}{\partial z}=-\frac{\partial p}{\partial r}+\frac{1}{r}\frac{\partial}{\partial r}(r\tau_{rr})-\frac{\tau_{\theta\theta}}{r}+\frac{\partial \tau_{rz}}{\partial z}$$

$$\frac{\partial \rho v}{\partial t}+\frac{1}{r}\frac{\partial \rho u v r}{\partial r}+\frac{\partial \rho v^2}{\partial z}=-\frac{\partial p}{\partial z}+\frac{1}{r}\frac{\partial}{\partial r}(r\tau_{rz})+\frac{\partial \tau_{zz}}{\partial z}$$

and

$$\frac{\partial \rho E}{\partial t}+\frac{1}{r}\frac{\partial \rho u r E}{\partial r}+\frac{\partial \rho v E}{\partial z}=-\frac{1}{r}\frac{\partial p u r}{\partial r}-\frac{\partial p v}{\partial z}+\frac{1}{r}\frac{\partial}{\partial r}\left(r k_f \frac{\partial T}{\partial r}\right)+\frac{\partial}{\partial z}\left(k_f \frac{\partial T}{\partial z}\right)+\frac{\partial}{\partial z}(\tau_{rz}u+\tau_{zz}v)+\frac{1}{r}\frac{\partial}{\partial r}[r(\tau_{rr}u+\tau_{rz}v)] \quad (1)$$

where u and v represent components in the radial and axial directions. Here, τ contains fluid stresses, including both laminar and turbulent effects, if any, and k_f is the fluid thermal conductivity. The required boundary conditions that maintain continuity of heat, mass, and momentum across the fluid–solid interface are

$$Q_{f,w}=Q_r=k_r\left(\frac{\partial T_r}{\partial n}\right)_w$$

$$T_w=T_r=T_f$$

$$\mathbf{u}=0|_w$$

and

$$p_r=p_f|_w \quad (2)$$

where w indicates quantities evaluated at the wall and subscripts r and f denote rock and fluid properties: for example, the thermal conductivity (k_r), the heat flux at the rock surface ($Q_w=Q_r$), and the rock temperature (T_r). The coordinate n signifies the direction perpendicular to the local surface rock contour. In addition, there must be flow and energy continuity and pressure equalization across the inlet nozzle flow boundary at the sonic point and the outlet boundary.

The constitutive relationships required to close the system of equations include an equation of state, here chosen to be that of a polytropic gas

$$p=(\gamma-1)\rho I \quad (3)$$

for which p/ρ^{γ} is a constant during an adiabatic process. In addition a relationship between fluid stresses and other measurable flow quantities is needed. If shearing rates or stresses are not too great, the fluid, particularly if it is a low density gas, can be expected to follow a simple law of proportionality between strain rate ($\partial u_i/\partial x_j+\partial u_j/\partial x_i$) and stresses. The 'constants' of proportionality, the bulk (λ) and shear (μ) viscosities, are also generally functions of temperature for a given fluid. Furthermore, for simple gases without internal degrees of freedom, the Stokes assumption, $3\lambda+2\mu=0$, is valid and provides a means of estimating bulk viscosity.

FINITE-DIFFERENCE FORMULATION

Because these equations cannot, in general, be solved analytically, numerical solution methods must be adopted. Finite-difference numerical methods rely on the assumption that the continuum may be divided into arbitrarily small sections, each of which must obey the constitutive and conservation laws posed previously [12]. In this case, derivatives are approximated by linear finite-difference equations, where all quantities are defined at the center of each cell (i, j). Naturally, the accuracy of these approximations depends strongly on the size of time and spatial increments, δt and δr, and on the exact manner of formulating finite-difference equations for that problem. The detailed representation of the differenced

equations for compressible fluid flow are available from many sources, including refs. [12, 13]. As in most high-speed flow simulations, upwind differencing techniques [13] are employed to maintain stability of the numerical solution. Furthermore, because of the explicit formulation, time step restrictions are imposed by the Courant limit $((|u|+c)\delta t/\delta x)$, where c is the local speed of sound.

The accuracy of the simulation is also governed by characteristics of the computational mesh used to solve fluid flow. Errors from nonorthogonality of cells and variable cell spacings can be partially overcome by refinement of the computational technique (for instance, mapping to a computational grid [13]), but our approach attempted to eliminate most errors by having cells in the mesh interior deviate only slightly from orthogonality. Cells along the rock wall exhibited some more deformation in order to conform to the curved rock–gas interface.

The curvature of the spalling surface must be approximated through piecewise linear functions to be consistent with finite-difference formulation. Two possible mesh-generating schemes are possible, both of which have inherent advantages for this simulation. In the first, the grid is formed to the contour of the rock surface. Cell connectivity near the drill and nozzle housing could be troublesome with this scheme, posing time step limitations by incorporating extremely small cells near the drill housing, and nonorthogonality of the mesh extends throughout the computational region. Transformation of coordinate systems from physical space to computational space reduces some difficulties associated with body-fitted meshes [13].

Furthermore, this avoids skewness of the flow to the mesh. As a result, because fluid tends to hug the rock wall within the wall jet, the diffusive nature of an upwind differencing scheme would be partially ameliorated by adopting this first technique [14]. However, uncertainties about grid structure in the nozzle outlet region and the added complexity of coordinate transformations are unattractive features of this method. Therefore, we chose the second option, a nominally uniform orthogonal grid conformed to the wall contour (Fig. 2).

As discussed by Amsden and Hirt [15], simple methods for generating curvilinear meshes are abundant. One of the easiest to use simply involves specifying boundary nodes, and allowing interior nodes to successively relax to fill the computational region with nominally uniform volume cells, prior to commencing actual simulation. Orthogonality of the majority of cells is preserved, and Courant restrictions on the time step size arising from extremely small cells are avoided. However, the near-wall region suffers some loss of accuracy but only in the diffusive flux terms. In order to maintain conservation of fluid properties to the best degree, finite-volume differencing was implemented. For example, the mass conservation equation

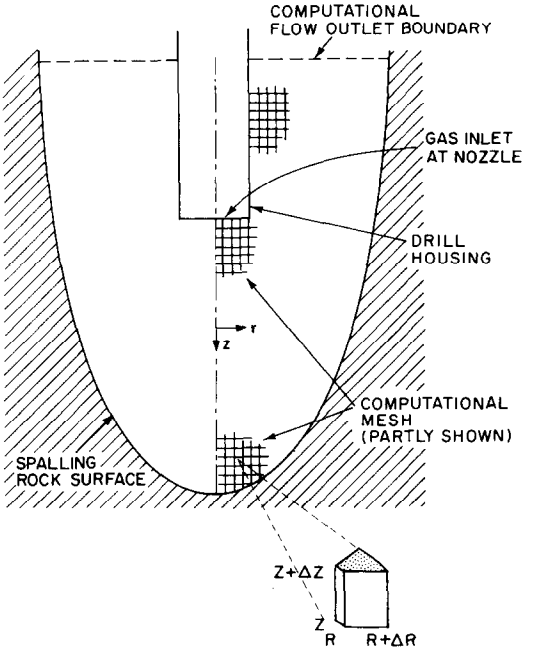

FIG. 2. Finite-difference computational mesh (partially shown) within simulated region bounded by inlet nozzle, rock surface, and annular flow outlet. Note the variable number of cells in the radial direction and that some cells along the spalling surface will have two sides on the rock–gas interface.

$$\frac{\partial \rho}{\partial t}+\frac{1}{r_{i,j}\delta r}[(ru:\rho)^{DC}_{i+1/2,j}-(ru:\rho)^{DC}_{i-1/2,j}]$$

$$+\frac{1}{\delta z}[(v:\rho)^{DC}_{i,j+1/2}-(v:\rho)^{DC}_{i,j-1/2}]=0 \quad (4)$$

reduces to

$$\frac{\partial \rho}{\partial t}+\frac{1}{V_{i,j}}\sum_{\substack{\text{cell}\\ \text{faces}}}[\rho^{DC}_{i,j}(uA_h+vA_v)]=0 \quad (5)$$

in which DC denotes quantities consistent with donor-cell (upwind) differencing, the quantities on the right of the colons are donored onto the quantities on the left, and A_h and A_v are horizontally and vertically projected facial areas on the four edges of the cell. Similar modifications can be imposed on the momentum and heat conservation equations by properly integrating fluxes in a finite-volume fashion.

Thus, to be consistent with the curved nature of the boundary, the grid architecture consists of rows with a variable number of cells in the radial direction and several cells across the fluid inlet from the sonic nozzle. Because the hole radius will be one of the parameters of most interest, enough cells are placed in the axial direction to ensure an adequate computational region to account for most of the spallation rock flux into the fluid. Therefore, the computed hole slope will be nearly vertical at the fluid exit. The modification of the mesh to conform to the boundary is then performed such that the interior points be at positions given by the average of their neighbors' loci. As was

demonstrated from a few initial runs, nearly all of the fluid forms a wall jet, and the boundary conditions on the drill housing are relatively unimportant. This indicated that we could have, in retrospect, used a different mesh construction, substituting one that hugged the wall and does not resolve the drill housing area as well. This should be explored further in another investigation. Nonetheless, the predominant emphasis will be focused on heat flux and fluid stresses in the compressible turbulent boundary layer wall jet flowing past the rock surface, which is assumed to be a hydrodynamically rough surface. Only implementation of boundary conditions needs to be addressed at this point.

DETERMINATION OF WALL HEAT FLUX AND TEMPERATURE BOUNDARY CONDITIONS

As demonstrated in refs. [1, 6], the proposed theory of rock spallation predicts, to first order, a direct dependence of rock penetration rate on applied heat flux. Dmitriyev *et al.* [16] and Gray [17] also assumed that such a relationship must be approximately valid, and Soviet spallation experiments have stockpiled an impressive amount of field data that indirectly supports this claim. As a complication to this otherwise exceedingly simple heat balance as a basis for determining rock spallation rate, the rock surface spallation temperature might be slightly affected by the amount of heat applied. Therefore, proper modeling of the drilling process is intimately linked to accurate prediction of heat transferred per unit time per unit area of rock surface for a variety of operating pressures, velocities, and geometries.

The details of the flow of a compressible, highly turbulent boundary layer resulting from an impinging, supersonic jet sweeping quickly past a somewhat roughened, ablating surface are not well understood. Furthermore, accurate resolution of boundary layer flow will be hindered by uncertainties in mesh construction and restrictions on grid size to give a reasonable number of cells. Roughness and asperities protruding into the boundary layer will negate the effectiveness of finer discretization of the flow. The simplest method in which to proceed would rely on previous studies of flows under similar conditions. However, as described below, previous investigations have been limited to flows that are not sufficiently similar to present circumstances. Thus, theoretical aspects of turbulent transport phenomena and compressible boundary layer flows will necessarily be investigated to generate a description of heat transfer at the spalling rock surface based somewhat more firmly on first principles.

The quantity of data reported in the literature for subsonic jets impinging on concave surfaces is fairly substantial [18–22], and flow patterns are well established, especially for jets impinging on flat plates [23–26]. However, the general heat transfer behavior of a single jet exhausting into an arbitrarily shaped concave body has not been adequately examined. Considerable doubt about the possibility of local heat flux maxima and the lack of data for high jet Reynolds numbers (above 10^5) accentuate the need for more fundamental studies and correlative work in this field. More importantly, impingement characteristics of supersonic jets are substantially different from those of subsonic, incompressible jets [27]. Specifically, shocks resulting from jet and ambient pressure equalization and contact with external bodies, such as plates or bluff objects, complicate the pressure and velocity fields. Furthermore, stagnation bubbles in impinging supersonic jet flows [28–30] can markedly affect the resulting plate heat transfer.

As a consequence, the only proposed method of computing heat transfer to flat plates from supersonic jets by Piesik and co-workers [31, 32] does not rely on the usual Nusselt number–Reynolds number relationships usually supplied for subsonic jet heat transfer. Piesik extended the generality of Nusselt number-based relationships for subsonic jet heat transfer by computing some of the jet expansion behaviour, thereby determining local gas properties in the plate boundary layer. In his model, given chamber conditions, the exit velocity, pressure, and full expansion conditions are specified through gas thermodynamic relationships. The Mach number decay along the centerline conforms to an experimentally determined power-law expression. Piesik chose to average the flow by assuming that within a 'constant core region', similar to that observed for subsonic jets but much lengthier, supersonic flow properties are constant. This ignores discrete perturbations around ambient pressure within shock cells, but static pressures within supersonic free jets have been found to be nearly equal to ambient after about four diameters downstream from the nozzle exit [27].

Piesik proceeded with a pseudo-finite-difference calculation of the plate flow, adding incoming, stagnating fluid as it enters the plate region with properties calculated from the expansion analysis. Ambient air is entrained as a function of the total flow in a manner that conserves total flow momentum. Then, empirically determined heat transfer correlations borrowed from Van Driest [33] are employed to estimate plate heat transfer coefficients. The predicted radial variation of heat transfer matches well with several unpublished, mostly qualitative plate heating data [31].

However, in relation to the current study, none of the currently available experimentally based methods for computing heat transfer from impinging jets is general enough to guarantee reliable predictive capability in the configuration of interest, that is, a supersonic, turbulent jet interacting with a concave, axisymmetric cavity, perhaps approximated by an ellipsoidal shape, formed by an ablating rock surface. All subsonic correlations given in the literature, except one [22], were applicable only to flat plate flows, and extension of predictions of these models to higher-speed jets is ill-advised [30]. In particular, no Nusselt–

Reynolds number relation has been proposed that satisfactorily describes supersonic heat transfer experimental data. Only Piesik's [31, 32] formulation has successfully predicted heat transfer from supersonic jet impingement, and even then, only spatially-averaged or time-integrated data have been quantitatively compared to his predictions. Furthermore, the assumptions on which his engineering treatment is based are contingent on flat-plate geometry. More fundamentally, flow pressures and velocities for a confined, reversing supersonic jet are not well documented, and in light of previous studies of lower-speed jets issuing into similar cavities, the possibility of establishing stable recirculation patterns and stagnation zones within the flow must be considered [18, 19]. Therefore, because the most reliable description possible of flame-jet heat transfer to a concave surface is sought, a more general approach to analyzing the expected turbulent jet aerodynamics is required in this case.

TURBULENCE MODEL EQUATIONS

In modeling turbulent flows, previous investigators have undertaken many varied approaches, and their respective advantages and drawbacks have been examined [5, 34, 35]. Turbulent flow is characterized by random fluctuations in system quantities (temperature, velocities, pressure) in the region of interest. Mean flow quantities can be defined as a time-averaged value, where the time of averaging is considerably smaller than the time-scale of the experimental study of macroscopic flow behavior. For instance, during a typical transient experiment, the time-scale for mean flow changes will be governed by dimensions of the test apparatus and the mean fluid velocity. However, the eddy length scale and fluctuating velocities will control the time scale for turbulent variations, which generally occur more rapidly than macroscopic flow transients. These velocity fluctuations will persist into steady state, if one exists, for the flow configuration under consideration. Thus, in order to mathematically describe the flow, total quantities are divided into time-averaged and fluctuating components, e.g.

$$u = \bar{u} + u', \quad v = \bar{v} + v', \quad p = \bar{p} + p'. \tag{6}$$

Substitution of the time-averaged and fluctuating components of velocity and pressure into the momentum equation, written in tensor form, yields

$$\frac{\partial \rho \bar{u}_i}{\partial t} + \frac{\partial \rho \bar{u}_i \bar{u}_j}{\partial x_j} = -\frac{\partial \bar{p}}{\partial x_i} + \frac{\partial}{\partial x_j}\left(\mu \frac{\partial u_i}{\partial x_j} - R_{ij}\right) \tag{7}$$

where $R_{ij} = \rho \overline{u_i' u_j'}$, the Reynolds stress tensor, contains fluid stresses arising strictly from flow field fluctuations. For all lower-order turbulence models, the Reynolds stress for incompressible flows is simply required to be proportional to the mean flow gradients, much in the same way that viscous stresses are described:

$$-\rho \overline{u_i' u_j'} = \mu_t \left[\frac{\partial u_i}{\partial x_j} + \frac{\partial u_j}{\partial x_i}\right] - \frac{2}{3}\rho k \delta_{ij}. \tag{8}$$

This approximation, first postulated by Boussinesq [36], only requires an expression for turbulent kinematic viscosity, μ_t and k, the turbulent flow kinetic energy ($k = \overline{u_i' u_i'}/2$) can be combined with the fluid pressure. In cases when eddy length scale descriptions are not reliable, these highly empirical models often fail. Many researchers have improved the range of applicability of these turbulence viscosity models by proposing models incorporating a differential equation for turbulent kinetic energy for use in eddy viscosity formulas and dissipation rate ε, derived from the Navier–Stokes equation and modeled by standard techniques [37]

$$\frac{\partial \rho k}{\partial t} + \frac{\partial \rho u_j k}{\partial x_j} = \frac{\partial}{\partial x_k}\left[\frac{\mu_t}{\sigma_k}\frac{\partial k}{\partial x_k}\right] - R_{ik}\frac{\partial u_i}{\partial x_k} - \varepsilon \tag{9}$$

$$\frac{\partial \rho \varepsilon}{\partial t} + \frac{\partial \rho u_j \varepsilon}{\partial x_j} = \frac{\partial}{\partial x_k}\left[\frac{\mu_t}{\sigma_\varepsilon}\frac{\partial \varepsilon}{\partial x_k}\right] - C_{\varepsilon 1}\frac{\varepsilon}{k}R_{ik}\frac{\partial u_i}{\partial x_k} - C_2\frac{\varepsilon^2}{k} \tag{10}$$

and the turbulent viscosity is found through dimensional considerations

$$\mu_t = C_\mu \rho \frac{k^2}{\varepsilon} \tag{11}$$

where σ_k, σ_ε, $C_{\varepsilon 1}$, and $C_{\varepsilon 2}$ are all of order unity and C_μ is about 0.1.

The difficulty in the actual application of these equations lies in approximations of nearly isotropic turbulence and determination of the constants, particularly in regions near the wall where the velocity component normal to the wall decays much more rapidly than that tangential to the wall. Generally, for well-defined configurations such as supersonic boundary layers on smooth flat plates or free axisymmetric jets, the k–ε model as stated is extremely useful for predicting flow behavior but only if extremely fine discretization is supplied near the confining boundary and some low turbulent Reynolds number modifications are added to the equations (such as the viscous term neglected from equation (10)) [37].

In the case at hand, heat and momentum transport to the rough, axisymmetric wall from high-speed, nearly sonic flow moving past it are crucial, and without fine zoning near the wall, details of the turbulent boundary layer would be confined to one or two cells without spending considerably more on computer time and storage. Launder and Spalding [37] foresaw this potential limitation to their method and, in addition to proposing the low Reynolds number modifications mentioned above, set forth a formulation that combined the traditional 'law-of-the

wall' velocity and temperature profiles with the two-equation turbulence model. Finite-difference formulations are easily established for both k and ε in the bulk of the computational mesh, but near a wall, because the differential equations are no longer valid in the laminar sublayer, law-of-the-wall profiles are inserted.

Launder and Spalding [37] proposed that the finite-difference grid be arranged such that the least computational cell has its center in the fully turbulent core of the boundary layer ($1 \ll y^+ < 1000$, $(k^2/\varepsilon\nu)_p \gg 1$, $y^+ = n\sqrt{(\tau_w\rho)}/\mu$ in which the subscript p denotes quantities defined at that cell's center). Furthermore, the dissipation ε_p at that point must always be proportional to $k_p^{3/2}/n_p$, where n_p is the distance from the cell center to the wall. Effectively, this constitutes a return to a mixing-length description for the structure of the boundary layer. Thus, some minor modifications to law-of-the-wall relations were suggested, and the final form of the equations to be solved is, for incompressible flow

$$\frac{u_p}{(\tau/\rho)_w} C_\mu^{1/4} k_p^{1/2} = \frac{1}{\kappa} \ln \frac{En_p(C_\mu^{1/4} k_p^{1/2})}{\nu} \tag{12}$$

$$\frac{(T_p - T_w)\rho C_p C_\mu^{1/4} k_p^{1/2}}{Q_w} = \frac{Pr_t}{\kappa} \ln \frac{En_p(C_\mu^{1/4} k_p^{1/2})}{\nu} \tag{13}$$

where

$$\varepsilon_p = C_\mu^{3/4} k_p^{3/2}/\kappa n_p. \tag{14}$$

The computation of k_p, which is still comparable to the mean flow turbulent kinetic energy, is to be performed in precisely the same manner as with all other finite-difference cells, and the power of the method permits determination of wall heat flux without fine discretization in the boundary layer. Two difficulties arise for extension to this application: the nature of the wall is very poorly understood, though some roughness is bound to be present, and the preceding development makes no account for compressibility effects.

COMPRESSIBILITY AND ROUGHNESS EFFECTS

Concerning the effect of compressibility in the boundary layer, Van Driest [38] considered the influence of property variations across the boundary layer due to temperature changes for high-speed ($M > 0.3$) flows. In particular, for a perfect gas with density ρ and temperature T, transformations can be introduced into the heat transfer equation, but all temperatures should now be defined as total, or stagnation, temperatures [38]. Launder and Spalding's velocity is replaced because of compressibility effects by Van Driest's generalized velocity, obtained from

$$\int_0^{u_\infty} \left(\frac{\rho}{\rho_w}\right)^{1/2} du = \frac{u_\infty}{A}\left[\sin^{-1}\left(\frac{2A^2(u_p/u_\infty) - B}{(B^2+4A^2)^{1/2}}\right) + \sin^{-1}\left(\frac{B}{(B^2+4A^2)^{1/2}}\right)\right] \tag{15}$$

where

$$A^2 = \frac{(\gamma-1)M_\infty^2}{2(T_w/T_\infty)} \tag{16}$$

and

$$B = \frac{1 + \dfrac{\gamma-1}{2} M_\infty^2}{T_w/T_\infty} - 1. \tag{17}$$

A form of the law of the wall more readily usable in Launder and Spalding's wall function approximations for both heat and momentum transfer is obtained reevaluating A and B at point p (using M_p and T_p rather than M_∞ and T_∞) and performing the integration of $(\rho/\rho_w)^{1/2}$ from $u = 0$ to u_p

$$\frac{u_p}{(\tau/\rho)_w} C_\mu^{1/4} k_p^{1/2} = \frac{A_p}{\kappa} \ln \frac{En_p(C_\mu^{1/4} k_p^{1/2})}{\nu_w}\left[\sin^{-1}\left(\frac{2A_p^2 - B_p}{(B_p^2+4A_p^2)^{1/2}}\right) + \sin^{-1}\left(\frac{B_p}{(B_p^2+4A_p^2)^{1/2}}\right)\right]^{-1}. \tag{18}$$

The subscript p will be dropped from the constants A and B hereafter for clarity. We then assume that the local heat flux perpendicular to the wall, Q_w, is found from a similarly modified form of equation (18). Our proposed use of Van Driest's generalization in the heat transfer wall function follows from the Reynolds analogy. In our simulations, y_p^+ was about 500–700 at all points in the region of greatest heat flux (near the hole bottom).

Viegas and Rubesin [39] have used a similar modification of the law-of-the-wall to compute predictions for local skin friction coefficients, momentum thicknesses, and displacement thicknesses in various shock–boundary layer interaction flows. With the modified law-of-the-wall, they were able to place the cell center next to the wall at y^+ between 80 and 1000, whereas the comparable runs using full integration to the wall often required the minimum y^+ to be about 0.5, generally using eight times the computer time. Surprisingly, matches with experimental data were often improved by use of the wall function over the full Navier–Stokes calculation, and separations of boundary layers after encountering shocks were predicted remarkably well.

Before equation (18) can be implemented in this study, the effects of wall roughness on the laminar

sublayer thickness must be examined. If $Re_c = h_c\sqrt{(\tau_w/\rho_w)}/\nu > 70$, where h_c is the asperity dimension, then the viscous layer will disappear entirely. Because the molecular Prandtl number is sufficiently close to unity, heat and momentum transfer are analogous down to the outer edge of the wall roughness, regardless of the existence of a laminar sublayer. More importantly, characteristics of the turbulent boundary layer may be changed by the presence of asperities on the rock surface, thereby altering constants in law-of-the-wall relations. In the case of heat transfer, they may change the resistance to heat transfer by introducing local pockets of stagnation.

As Chen [40] states, necessary modifications to the law of the wall arise from a change in mechanism in transfer of momentum and heat to the wall. The mixing length $l = \kappa n$ cannot become zero as n goes to zero, since dynamic pressure from the impact of fluid on each roughness element contributes significantly to drag on the gas. Now, $l = \kappa(n + Ch_c)$, where h_c is the average size of roughness perpendicular to the wall and C has been experimentally determined as 0.031 [41]. Thus, the mixing-length at the contact locus is considerably smaller than the asperity dimension but does not vanish. Therefore

$$u^+ = \frac{1}{\kappa}\left[\ln y^+ + \ln\frac{32.6}{Re_c}\right] \tag{19}$$

and because Re_c is about 50–100 for this application, assuming an average roughness dimension of 0.5 mm, the increase in predicted shear stress is dramatic and the laminar sublayer almost vanishes. Comparison with equation (12) reveals that $E = 32.6/Re_c$, and equation (18) still produces a direct relationship for τ_w/ρ_w.

The analogy between heat and momentum transfer fails in this instance because isolated pockets of relatively stagnant fluid impede conduction of heat to the surface, and no comparable mechanism exists in the case of momentum transfer. Denoting St_c^{-1} as the reciprocal Stanton number for heat transfer though this semi-stagnant layer (which can be thought of as a lower limit on T^+ at the roughness cavities, defined as δT_0^+), Dipprey and Sabersky [42] let

$$St_c^{-1} = C\,Re_c^p\,Pr^q \tag{20}$$

and found for various sand-type roughnesses that

$$St_c^{-1} = 5.19 Re_c^{0.2}\,Pr^{0.44}. \tag{21}$$

Because the turbulence Reynolds analogy is valid down to the tip of the asperities, then

$$T^+ = \delta T_0^+ + \frac{Pr_t}{\kappa}\ln\frac{n}{h_c} \tag{22}$$

and

$$\delta T_0^+ = \frac{\rho C_p\sqrt{(\tau_w/\rho)}}{h_\delta} = St_c^{-1} = 5.19 Re_c^{0.2}\,Pr^{0.44} \tag{23}$$

in which h_δ is the effective heat transfer coefficient across the roughness element, adjusting the denominator of the heat transfer analog of equation (18) to read $(Pr_t/\kappa)[\ln(n/h_c) + St_c^{-1}]$. In this case, F in that relation can be about 1.0, but resistance added by molecular conduction through small pockets of fluid must be included.

Chen [40] reported excellent agreement in predicting compressible flow along a rough, convex hemisphere, using similar compensations for roughness factors, even though they were originally formulated for incompressible fluids. In addition, law-of-the-wall modifications were fairly independent of heating rate.

HEAT FLUX BOUNDARY CONDITION

The heat flux at each boundary cell can be specified as Q_w as given by the heat transfer equation formed from equations (13), (18), (22), and (23). Therefore, from the modified law-of-the-wall description for compressible turbulent flow over a roughened surface

$$Q_w = \frac{(T_p - T_w + \frac{1}{2}u_p^2/C_p)\rho C_p C_\mu^{1/4} k_p^{1/2}}{\frac{Pr_t}{\kappa}\ln\frac{Fn_p}{h_c} + 5.19 Pr^{0.44}\,Re_c^{0.2}}\frac{1}{A}$$

$$\times\left[\sin^{-1}\frac{2A^2 - B}{(B^2+4A^2)^{1/2}} + \sin^{-1}\frac{B}{(B^2+4A^2)^{1/2}}\right] \tag{24}$$

with A and B computed from equations (16) and (17) after substituting Mach number and temperature evaluated in the first cell away from the wall. The surface temperature T_w is given as

$$T_w = T_{ro} + \left[\left(\frac{Q_w}{(\rho C_p)_r}\right)^3\left(\frac{(1-\nu)\sigma_0}{\beta_r E}\right)^m\left(\frac{2(0.693)}{\pi C_L^2}\right)\left(\frac{m}{\sigma_r}\right)^3\right]^{1/(m+3)} \tag{25}$$

which results from the use of Weibull's statistical failure theory to estimate rock spallation temperature [1, 5, 6]. This expression neglects any fluctuations of rock surface temperature resulting from discrete chip formation. The wall is assumed to remain at spalling temperature, and the computed heat flux will slightly underestimate the actual value. In reality, the surface temperature of the next chip to be spalled must rise from that present on the backside of the previous spall to that specified by equation (25). The predictive capability of the simulation is not severely affected by the approximately 10% potential change in the temperature driving force between the bulk fluid and rock wall temperatures. The heat flux from equation (24) corresponds to that which induces rock spallation at a surface spallation temperature given by equation (25). Evaluation of Q_w demands an iterative calculation at each boundary cell until the wall temperatures given by equations (24) and (25) agree to within an accepted tolerance. Details of this calculation are provided in ref. [5].

The effect of shock waves on the spallation mech-

anisms are taken to be negligible at these low fluid pressures (~1 MPa compared with a nominal rock strength of over 100 MPa). Also, the additional energy required to form new rock surfaces has been shown elsewhere [5] to be several orders of magnitude less than the required energy input by the flame to raise the rock temperature until thermal failure is induced.

DESCRIPTION OF SIMULATION STRUCTURE AND PARAMETER NONDIMENSIONALIZATION

At this point, all wall boundary conditions have been specified. Within a simulation run, after specification of the beginning mesh and boundary conditions and initial fluid flow quantities, such as pressure and internal energy, transport effects are computed in three distinct steps: a Lagrangian phase in which cells are presumed to move with the fluid, an advective step that transports material across cell boundaries by repositioning the cell coordinates at their starting locations, and a diffusive/conductive phase [43]. Once steady-state velocity and temperature profiles are obtained, heat flux can be estimated to determine spalling rate at each location along the rock–fluid interface and the mesh is adjusted accordingly, as described below. Calculation proceeds once again until a new fluid flow steady state is reached in the adapted mesh, and the procedure repeats [5].

The input variables that most strongly affect the simulated gas dynamics are expressed in dimensionless form to facilitate presentation of results. These parameters include inlet pressure, temperature, velocity, turbulence level, and certain geometrical factors. From dimensional analysis of the conservation equations, turbulent transport relations, and boundary conditions, the following dimensionless groups emerge:

$$\frac{v_{\text{jet}}}{c_{\text{jet}}}, \frac{p_{\text{jet}}}{p_0}, \frac{I_{\text{jet}}}{C_t T_{\text{r0}}}, \frac{k_{\text{jet}}^{1/2}}{c_{\text{jet}}}, \frac{l_t}{R_{\text{dr}}},$$

$$\frac{Q_{\text{w}}}{(\rho C_p v)_{\text{jet}}(T_{\text{jet}} - T_{\text{r0}})}, \frac{\tau_{\text{w}}}{p_0}, Pr_t, \frac{R_{\text{h}}}{R_{\text{dr}}}$$

and the turbulent Prandtl number is hereafter taken as 1.0. Since the sonic nozzle outlet coincides with the inlet boundary of the simulation, the Mach number ($v_{\text{jet}}/c_{\text{jet}}$) is always set to 1.0. Furthermore, a constant ratio of rock heat capacity to gas heat capacity was used in all simulation runs. Therefore, the remaining dimensionless inlet parameters are a pressure ratio, a temperature ratio, the appropriately non-dimensionalized turbulent length scale, and the incoming turbulent energy (k_{jet}) as a fraction of mean flow kinetic energy.

However, incoming turbulence, aside from not being completely and independently adjustable, decays extremely rapidly during simulation runs. Consequently, its effects are ignored throughout the parameterization of process variables. Because wall heat flux determines the rock drilling rate and hole shape, calculation of wall shear stress is not the primary concern of this simulation. Thus, the effects of independent parameters (inlet pressure ratio, inlet temperature ratio) on heat flux (equivalently, drilling rate) are studied by conducting simulations that vary one parameter while holding the other inlet quantity fixed. Once jet pressure, temperature, and nozzle radius are specified, mass flow rate and energy flux from the jet are not independently adjustable and are directly obtainable by computation of jet density and velocity:

$$m^* = \frac{\rho_{\text{jet}} v_{\text{jet}} R_{\text{dr}}^2}{\rho_0 [C_t T_{\text{r0}}]^{1/2} Z_{\text{dr}}^2}. \tag{26}$$

The geometrical quantities of interest, which can be considered to characterize the configuration of the drilling process given gas and fuel flows and pressure, require some additional explanation. The standoff distance (Z_{dr}), the hole radius (R_{h}), and the drilling velocity (V_{dr}) are, strictly speaking, the three parameters that would be determined in any field drilling exercise. Not all of these parameters are independent, however, and, in practice, one of these quantities must be fixed. In the field, the easiest and most practical policy would adopt an established drilling rate within reasonable bounds (say, 0.0008–0.008 m s^{-1} (10–100 ft. h^{-1}), depending on rock type). In modeling spallation, the situation is more constrained, reducing the degrees of freedom available. Both local rock penetration velocity and overall hole dimension, which is directly related to the collective contributions of rock removal at each point, are unique functions of heat flux delivered to the surface and indirectly of surface temperature, ambient temperature, and rock properties, i.e. $u_{\text{r}} = f(Q_{\text{w}})$ and $R_{\text{h}} = g(Q_{\text{w}})$. Therefore, one of the preceding list of three parameters can be specified.

From a computational standpoint, relative standoff distance is much easier to set than either drilling velocity or hole radius. Standoff distance is difficult to specify a priori in the field, but fixing its value in conjunction with inlet flows does uniquely determine drilling rate and hole radius. The heat flux that computationally controls the drilling velocity is not particularly sensitive to the exact value of hole radius since the majority of heat transfer occurs near the hole bottom. However, standoff distance and heat flux are quite strongly linked and allowing these two sensitive parameters to adjust throughout the simulation creates unstable behavior, as seen in some trial runs. Each boundary cell is forced to conform to a self-consistent hole shape through adjustment of the inclination angles measured from the horizontal of the boundary cells that indirectly determines overall hole size

$$u_{ri} \equiv V_{\text{dr}} \cos\theta_i = f(Q_{\text{w}i}, T_{\text{w}i}); \quad R_{\text{h}} = \sum_{\text{cell}} l_i \cos\theta_i \tag{27}$$

where i signifies a boundary cell side of length l_i, and $T_{\text{w}i}$ is a function of rock properties and the local heat

flux Q_{wi}. If drilling rate were specified instead of standoff distance, equation (27) would also, in effect, determine hole radius. In that case, evaluation of the correct standoff distance to be tried in the next rezoning of the mesh would not be so straightforward, however. For example, suppose that heat flux at the hole bottom were too high for the preset drilling speed. If increasing standoff distance did not improve this discrepancy, then correct nozzle placement would be uncertain.

If hole radius and standoff distance are nondimensionalized with variables already presented, then the following final list of three independent and two dependent parameters emerges

$$\frac{I_{\text{jet}}}{C_u T_{r0}}, \frac{p_{\text{jet}}}{p_0}, \frac{Z_{\text{dr}}}{R_{\text{dr}}}, \frac{R_{\text{h}}}{R_{\text{dr}}}, \frac{Q_{\text{w}}}{(\rho C_p v_{\text{jet}})(T_{\text{jet}} - T_{r0})}$$

for gas inlet parameters and from geometrical effects. As discussed in ref. [1], a direct correspondence exists between applied surface heat flux and local penetration rate u_r

$$Q_{\text{w}} = (\rho C_p)_r u_r (T_{\text{w}} - T_{r0}) \tag{28}$$

which can be used to modify the form of the wall heat flux–jet heat flux dependent parameter. If we define $\langle Q_{\text{w}} \rangle$ as that heat flux required to cause an overall drilling velocity V_{dr} then

$$\frac{\langle Q_{\text{w}} \rangle}{(\rho C_p v)_{\text{jet}}(T_{\text{jet}} - \langle T_{\text{w}} \rangle)} \equiv \frac{(\rho C_p)_r V_{\text{dr}}(\langle T_{\text{w}} \rangle - T_{r0})}{(\rho C_p v)_{\text{jet}}(T_{\text{jet}} - \langle T_{\text{w}} \rangle)}. \tag{29}$$

If all sections of the computed hole shape were consistent with a drilling velocity V_{dr}, then, at each point, $u_r = V_{\text{dr}} \cos\theta$. A proper average for $\langle Q_{\text{w}} \rangle$ may be defined by averaging the normalized heat flux $Q_{\text{w}}/\cos\theta$ over a reasonable but arbitrary number of computational boundary cells (here taken to be those cells with $\theta_i < 45°$). Given a self-consistent hole, the shape of all $Q_{\text{w}}/\cos\theta$ values will be identical. Averaging these values merely provides a smoothed estimate of the drilling velocities. Rock properties other than heat capacity, such as Young's modulus and failure strength, must also be considered, though for the purposes of all subsequent discussions, only the effects of these on T_{w}, the rock spalling temperature, will be considered

$$\frac{T_{\text{w}}}{T_{r0}} = f\left[\left[\frac{(1-\nu)\sigma_0}{\beta_r E T_{r0}}\right]^m \left(\frac{V_{\text{dr}}}{\sigma_r}\right)^3, C_L\right]. \tag{30}$$

This parameterization of the rock drilling results in terms of input quantities provides a clear way of analyzing the expected trends.

PRESENTATION OF RESULTS AND EXPECTED TRENDS

In Figs. 3 and 4, the graphs summarizing the results of all simulation runs illustrate expected trends in field performance of the spallation drill in response to process variable changes. The effective Stanton

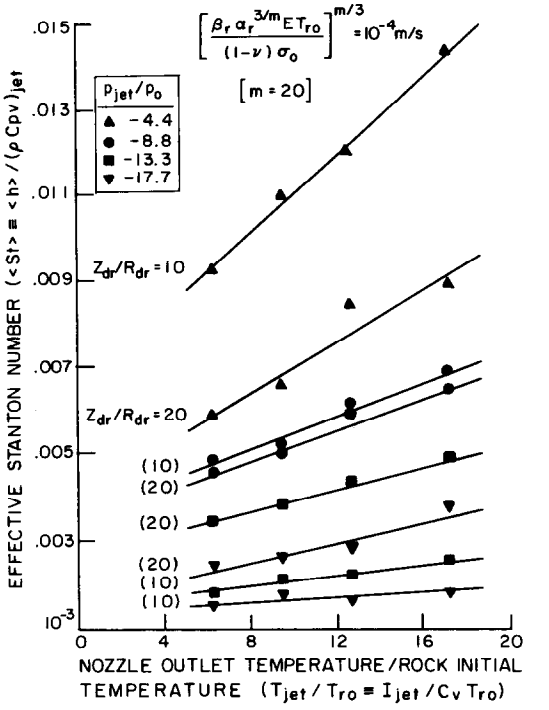

FIG. 3. Computed effective Stanton number (symbols) vs inlet temperature ratio with standoff distance and inlet pressure ratios as parameters.

number, $\langle h \rangle_{\text{eff}}/(\rho C_p v)_{\text{jet}}$, can be physically interpreted as the ratio of heat transferred to the surface within the arbitrary limit of 45° inclination (normalized to account for the local angle as discussed above with $\langle Q_{\text{w}} \rangle = (\rho C_p)_r V_{\text{dr}}(\langle T_{\text{w}} \rangle - T_{r0})$) to the jet heat flux entering from the sonic nozzle, using the average

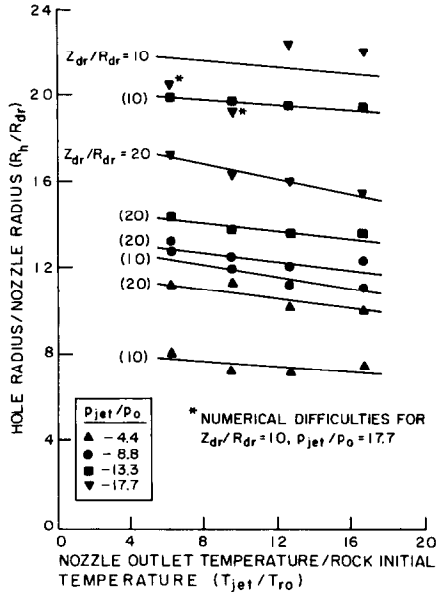

FIG. 4. Computed dimensionless radius (symbols) vs inlet temperature ratio with standoff distance and inlet pressure ratios as parameters.

rock spallation temperature as a standard reference ($Q_{jet} = (\rho C_p v)_{jet}(I_{jet}/C_v - \langle T_w \rangle)$). The depicted rise in its value as jet temperature rises may be misleading, however (Fig. 3). For choked flow at the nozzle exit, which was used in all simulations, v_{jet} contains a direct dependency on jet temperature ($v_{jet} \propto T_{jet}^{1/2}$), as dictated from fluid thermodynamics and the local speed of sound at the nozzle throat temperature. However, at constant jet pressure, density (ρ_{jet}) falls as T_{jet}^{-1}. Therefore, the effective heat transfer coefficient $\langle h \rangle$ actually diminishes slightly with higher inlet temperature, especially at higher combustion pressures. The added flame temperature does compensate to produce an enhanced anticipated drilling rate, however. As Fig. 4 illustrates, non-dimensional hole radius can be expected to shrink with increasing flame temperature, given all other parameters to be equal (jet pressure, standoff distance, initial rock temperature). If mass flow rate is held constant, nozzle radius must grow as $T_{jet}^{1/4}$, and the net effect could be a slightly wider hole.

As also seen in Fig. 3, jet pressure at the throat of the nozzle has a somewhat peculiar effect on predicted drilling effectiveness. If standoff distance is low, at moderate pressures ($p_{jet}/p_0 < 9$) the directed nature of the jet remains intact, and the characteristics of the impingement resemble those expected for flat plate flows in which the heat flux monotonically diminishes from the flow centerline. As chamber (and nozzle) pressure is increased, however, a sort of flow reversal and stagnation 'bubble' is generated, previously unreported in the literature and quite different from those noticed in well-defined supersonic jets contacting flat plates [5, 28]. At these conditions, the expected trend of increased drilling rate with closer nozzle to hole bottom spacings is reversed. Faster drilling results at slightly larger standoff distances ($Z_{dr}/R_{dr} \geqslant 10$). Advancing the drill any faster leads to an operational instability. That is, at certain standoff distances, any perturbation that momentarily raises the penetration rate of the burner will only serve to decrease the bottom hole heat flux, diminishing rock removal rate and further shortening drill standoff. This phenomenon of flow reversal at high incoming pressures is expected to hold for dimensionless standoff distances (Z_{dr}/R_{dr}) less than about 20. At higher standoff distances from the hole bottom, heat transfer rates will decline further. From Fig. 4, for low pressure jets larger holes are favored as dimensionless standoff distance is increased from 10 to 20. This trend reverses at higher pressures. The effect is reduced somewhat if mass flow rate is fixed, while pressure is varied. Since nozzle radius will, in that case, decrease as $p_{jet}^{1/2}$, higher pressures may induce only a slight increase in hole radius.

As noted above, given a relatively low standoff distance of about 10, the average penetration rate $\langle Q_w \rangle$, the representative mean heat flux, could actually be higher for a lower pressure jet. Thus, an optimal standoff distance exists, above or below which the predicted penetration rate will fall. For instance, for the lowest pressure jets examined, maintaining a lower standoff should give better drilling rates within parameter limits tested in this study. From practical considerations, however, the standoff distance would self-adjust during a field drilling operation to be consistent with the actual penetration rate of the flame-jet drilling assembly.

Extremely wide holes are predicted with progressively less accuracy (starred points on Fig. 4), since the inevitable expansion of computational cells near the wall as the hole enlarges reduces calculational reliability. Thus, little confidence is placed on the exact location of the line on Fig. 4 corresponding to $p_{jet}/p_0 = 17.7$, $Z_{dr}/R_{dr} = 10$, but indications are that it should lie above that for $p_{jet}/p_0 = 13.3$ at the same standoff. Adaptive grids capable of repositioning cells within the mesh to regions of lower accuracy or steeper property gradients will enhance the precision of future predictions under high pressure-low standoff conditions. Nonetheless, the trends are not expected to be noticeably different but should be corroborated in the field by piercing with high-pressure flame-jets under controlled conditions.

Two calculations performed with twice the mesh points in each direction produced very similar results, with about 10% higher surface heat flux directly below the jet exit and about the same hole radius. While this is not exact numerical convergence, we are predicting bottom hole heat fluxes that are within 20–30% of those expected at the limit of zero mesh size.

CONCLUSIONS AND RECOMMENDATIONS

A finite-difference fluid dynamics model has been written that is capable of predicting spallation drilling rates and hole sizes under a variety of operating conditions. The model incorporates fluid turbulence effects on the heat transfer rate to the hydrodynamically rough rock surface. It is this heating rate that directly determines rock spallation velocity and indirectly sets hole shape. Experiments testing the accuracy of the code will be discussed in Part 2 of this paper.

Several areas that need improvement within the model should be mentioned. Although the effects of spalls on the mean flow field are shown to be negligible in other work [5], the potential influence of chips on the fluid turbulence has been ignored here. Also, to quicken runtimes, because the steady-state condition is the only one of interest, the largest allowable time step for each cell should be taken locally rather than limit δt by the smallest Courant number in the entire mesh. Therefore, although the simulation would not be time-accurate, the procession to steady state would occur much more rapidly by flushing errors more quickly out of the system. In addition, the potentially deleterious effects of excess numerical diffusion introduced by upwind differencing could be lessened [14] by introducing higher-order differencing schemes. However, for the purposes of recognizing trends pre-

dicted by the model, the accuracy of the techniques used here should be sufficient.

Acknowledgements The authors wish to thank Francis H. Harlow and Robert M. Potter of Los Alamos National Laboratory and Mark Wilkinson, Kenneth Smith, and Michael Manning of MIT for their guidance and timely ideas concerning this project.

REFERENCES

1. R. M. Rauenzahn and J. W. Tester, Rock failure mechanisms of flame-jet thermal spallation drilling: theory and experimental testing, *Int. J. Rock Mech. Geomech. Abstr.* **26,** 381–399 (1989).
2. H. C. H. Armstead and J. W. Tester, *Heat Mining.* Chapman & Hall, London (1986).
3. D. E. Fogelson, Advanced fragmentation techniques, 3rd Congr. Int. Soc. Rock Mech. (1974).
4. L. B. Geller, A new look at thermal rock fracturing, *Trans. Inst. Min. Metall.* **79,** A133–A170 (1970).
5. R. M. Rauenzahn, Analysis of rock mechanics and gas dynamics of flame-jet thermal spallation drilling, Ph.D. Thesis, Mass. Inst. of Technol. (1986).
6. T. N. Dey, More on spallation theory, Los Alamos National Laboratory Internal Memorandum No. ESS-3-286-84 (1984).
7. J. A. Browning, W. B. Horton and H. L. Hartman, Recent advances in flame jet working of minerals, 7th Symp. Rock Mech., Pennsylvania State University, Society of Mining Engineers (1965).
8. J. A. Browning, Flame-jet drilling in Conway, NH, granite, unpublished report of work done under University of California order number 4-L10-2889R-1 for Los Alamos National Laboratory (1981).
9. P. G. Hill and C. R. Peterson, *Mechanics and Thermodynamics of Propulsion.* Addison-Wesley, Reading, Massachusetts (1965).
10. Ya. M. Paushkin, *The Chemical Composition of Properties of Fuels for Jet Propulsion.* Pergamon Press, Oxford (1962).
11. S. S. Penner, *Chemistry Problems in Jet Propulsion.* Pergamon Press, Oxford (1957).
12. F. H. Harlow and A. A. Amsden, Fluid dynamics, Los Alamos Scientific Laboratory Report LA-4700 (1971).
13. D. A. Anderson, J. C. Tannehill and R. H. Pletcher, *Computational Fluid Mechanics and Heat Transfer.* McGraw-Hill, New York (1984).
14. G. D. Raithby, Skew upstream differencing schemes for problems involving fluid flow, *Comput. Meth. Appl. Mech. Engng* **9,** 153–164 (1976).
15. A. A. Amsden and C. W. Hirt, A simple scheme for generating general curvilinear grids, *J. Comp. Phys.* **11,** 348–359 (1973).
16. A. P. Dmitriyev, I. D. Kill', A. K. Sukhanov and O. N. Tret'yakov, Calculating the parameters of the thermal drilling process, *Sov. Min. Sci.* **5,** 26–31 (1969).
17. W. M. Gray, Surface spalling by thermal stresses in rocks, Rock Mech. Symp., Toronto University, Mines Branch, Department of Mines and Technical Surveys (1965).
18. M. Maeda and K. Ohmori, Heat transfer of jet impinging on a V-shape inverse wedge, *J. Chem. Engng Japan* **13,** 194–198 (1980).
19. Ye. P. Dyban and A. I. Mazur, Heat transfer from a flat air jet flowing into a concave surface, *Heat Transfer—Sov. Res.* **2,** 15–20 (1970).
20. D. E. Metzger, T. Yamashita and C. W. Jenkins, Impingement cooling of concave surfaces with lines of circular air jets, *J. Engng Pwr, Trans. ASME* Series H91, 149–158 (1969).
21. R. E. Chupp, H. E. Helms, P. W. McFadden and T. R. Brown, Evaluation of internal heat-transfer coefficients for impingement-cooled turbine airfoils, *J. Aircraft* **6,** 203–208 (1969).
22. J. N. B. Livingood and J. W. Gauntner, Heat transfer characteristics of a single circular air jet impinging on a concave hemispherical shell, NASA TM X-2859 (1973).
23. P. Hrycak, Heat transfer from a row of impinging jets to concave cylindrical surfaces, *Int. J. Heat Mass Transfer* **24,** 407–419 (1981).
24. J. W. Gauntner, J. N. B. Livingood and P. Hrycak, Survey of literature on flow characteristics of a single turbulent jet impinging on a flat plate, NASA TN D-5652 (1970).
25. Cz. O. Popiel, Th. H. van der Meer and C. J. Hoogendoorn, Convective heat transfer on a plate in an impinging round hot gas jet of low Reynolds number, *Int. J. Heat Mass Transfer* **23,** 1055–1068 (1980).
26. K. Kataoka, H. Shundoh, H. Matsuo and Y. Kawachi, Characteristics of convective heat transfer in nonisothermal, variable-density impinging jets, *Chem. Engng Commun.* **34,** 267–275 (1985).
27. R. S. Snedeker and C. duP Donaldson, Experiments on free and impinging underexpanded jets from a convergent nozzle, *Aeronaut.* Res. Assoc. Princeton Report No. ARAP-63 (1964).
28. G. T. Kalghatgi and B. L. Hunt, The occurrence of stagnation bubbles in supersonic jet impingement flows, *Aeronaut. Q.* **27,** 169–185 (1976).
29. P. J. Lamont and B. L. Hung, The impingement of underexpanded, axisymmetric jets on perpendicular and inclined flat plates, *J. Fluid Mech.* **100,** 471–512 (1980).
30. I. A. Belov, I. P. Ginzburg and L. I. Shub, Supersonic underexpanded jet impingement upon flat plate, *Int. J. Heat Mass Transfer* **16,** 2067–2076 (1973).
31. E. T. Piesik, D. J. Roberts and H. Dershin, Final Report: Rocket Exhaust Impingement Study, CR-6-332-762-001, General Dynamics (1968).
32. E. T. Piesik and D. J. Roberts, A method to define low-altitude rocket exhaust characteristics and impingement effects, *J. Spacecraft* **7,** 446–451 (1970).
33. E. R. Van Driest, The problem of aerodynamic heating, *Aeronaut. Engng Rev.* **15,** 26–41 (1956).
34. W. C. Reynolds, Computation of turbulent flows, *Ann. Rev. Fluid Mech.* **8,** 183–203 (1976).
35. M. Hirata, H. Tamaha, H. Kawamura and N. Kosagi, Heat transfer in turbulent flows, Seventh Int. Heat Transfer Conf., Munich, F.R.G. (1982).
36. J. Boussinesq, Essai sur la Theorie des Eaux Courantes, *Mem. Presentes Acad. Sci.* **23,** 46 (1877).
37. B. E. Launder and D. B. Spalding, The numerical computation of turbulent flows, *Comput. Meth. Appl. Mech. Engng* **3,** 269–289 (1974).
38. E. R. Van Driest, Turbulent boundary layer in compressible fluids, *J. Aeronaut. Sci.* **18,** 145–160 (1951).
39. J. R. Viegas and M. W. Rubesin, Wall-function boundary conditions in the solution of the Navier–Stokes equations for complex compressible flows, Paper No. AIAA-83-1694, AIAA Fluid and Plasma Dynamics Conf. (1983).
40. K. Chen, Compressible turbulent boundary-layer heat transfer to rough surfaces in pressure gradient, *AIAA J.* **10,** 623–630 (1972).
41. M. M. Pimenta, The turbulent boundary layer: an experimental study of the transport of momentum and heat with the effect of roughness, Ph.D. Thesis, Stanford University (1975).
42. D. F. Dipprey and R. H. Sabersky, Heat momentum transfer in smooth and rough tubes at various Prandtl numbers, *Int. J. Heat Mass Transfer* **6,** 329–353 (1963).
43. A. A. Amsden and C. W. Hirt, YAQUI: an arbitrary Lagrangian–Eulerian computer program for fluid flows at all speeds, Los Alamos Scientific Laboratory Report LA-5100 (1973).

SIMULATION NUMERIQUE ET ESSAIS DU PERCAGE PAR DELITEMENT THERMIQUE A L'AIDE D'UN JET DE FLAMME—1. DEVELOPPEMENT DU MODELE

Résumé—Certaines roches polycristallines se fracturent en fragments selon des disques minces quand elles sont exposées à un chauffage rapide en surface. Des méthodes de perçage utilisant des jets de flamme comme source de chaleur exploitent ce comportement pour la mise en forme efficace du granit. Des extensions récentes de la théorie de Weibull à l'analyse du délitement des roches sont utilisées pour estimer les distributions des tailles des fragments et les températures de surface au début du délitement. Un code numérique de simulation du perçage qui tient compte du critère de fracture et des effets de la turbulence d'écoulement est développé pour prédire les vitesses de délitement et les rayons de perçage dans les conditions opératoires de perçage. Comme il est nécessaire d'avoir une bonne description du jet turbulent en paroi, la méthode de fonction pariétale est généralisée pour tenir compte de la compressibilité de l'écoulement sur des surfaces rugueuses non adiabatiques.

NUMERISCHE SIMULATION UND ERPROBUNG EINES BOHRVERFAHRENS AUF DER GRUNDLAGE DES TEMPERATURBEDINGTEN ABPLATZENS VON MATERIALIEN IN EINEM FLAMMSTRAHL—1. ENTWICKLUNG DES MODELLS

Zusammenfassung—Bestimmte polykristalline Gesteine zerfallen in dünne, scheibenähnliche Fragmente, wenn sie einer schnellen Oberflächenerwärmung ausgesetzt werden. In einigen gängigen Verfahren zur Herstellung von Bohrlöchern in hartem Fels werden Überschall-Flammstrahlen als Wärmequellen verwendet. Damit wird es möglich, das erwähnte Verhalten in Granitsteinbrüchen und zur Herstellung von Bohrlöchern auszunutzen. Die Theorie von Weibull über Fehlstellen im Gestein wurde jüngst erweitert, wodurch eine quantitative Analyse von Abplatzvorgängen an Fels möglich wurde. Dieses Verfahren wird zur Bestimmung der Größenverteilung der abgeplatzten Teilchen verwendet, außerdem zur Ermittlung der Oberflächentemperatur bei Beginn des Abplatzens. Es wird ein numerisches Verfahren zur Simulation des Bohrvorgangs entwickelt, das die Kriterien für Fehlstellen im Fels und Einflüsse der turbulenten Strömung berücksichtigt und die Berechnung der Abtraggeschwindigkeit sowie der Bohrlochdurchmesser unter realen Bedingungen ermöglicht. Da eine genaue Beschreibung des Wärmeübergangs beim Auftreffen eines turbulenten Strahls auf eine Wand erforderlich ist, wird das Verfahren der Wandfunktion in grober Weise verallgemeinert, was die Berücksichtigung der kompressiblen Strömung an aufgerauhten nichtadiabaten Felsoberflächen ermöglicht.

ЧИСЛЕННОЕ МОДЕЛИРОВАНИЕ И ОПЫТНЫЕ ИССЛЕДОВАНИЯ СТРУЙНО-ФАКЕЛЬНОГО ТЕРМИЧЕСКОГО БУРЕНИЯ—1. РАЗРАБОТКА МОДЕЛИ

Аннотация—Некоторые поликристаллические породы при воздействии интенсивного нагрева поверхности дробятся на тонкие дискообразные осколки. В ряде современных методов бурения твердых пород, использующих в качестве источников тепла сверхзвуковые струи, эта закономерность используется при эффективной добыче гранита или образовании взрывной скважины. Сделанные недавно уточнения теории Вейбулла о разрушении пород с целью качественного анализа их расщепления применяются для оценки распределений размеров осколков и температур поверхности породы при возникновении расщепления. Для определения скоростей разрушения и радиусов скважины в натурных условиях бурения разработан код численного моделирования бурения, включающий критерии разрушения породы и эффекты турбулентного течения. Поскольку необходимо точное описание теплопереноса через пристенную турбулентную струю, метод пристеночных функций приближенно обобщается для учета обтекания ожимаемой жидкостью шероховатых неадиабатических поверхностей породы.